Tailoring carbon nitride framework to improve the catalytic efficiency of the stabilised Palladium atoms

Evgeniya Vorobyeva,[a] Zupeng Chen,[a] Sharon Mitchell,[a] Rowan K. Leary,[b] Paul Midgley,[b] Roland Hauert,[c] Edvin Fako,[d] Núria López[d] and Javier Pérez-Ramírez*[a]

a.Institute for Chemical and Bioengineering, Department of Chemistry and Applied Biosciences, ETH Zurich, Vladimir-Prelog-Weg 1, 8093 Zurich, Switzerland. E-mail: jpr@chem.ethz.ch

b.Department of Materials Science and Metallurgy, University of Cambridge, CB3 0FS Cambridge, United Kingdom.

c.EMPA, Uberlandstrasse 129, CH-8600 Dubendorf, Switzerland.

d.Institute of Chemical Research of Catalonia (ICIQ) and Barcelona Institute of Science and Technology, Av. Països Catalans 16, 43007 Tarragona, Spain.

Graphitic carbon nitride (g-C_3N_4) exhibits unique properties for the preparation of single-atom heterogeneous catalysts (SAHCs) due to the presence of sixfold nitrogen-based coordination sites in the lattice. Despite the potential to profoundly affect the electronic and related catalytic properties of the metal, no work has attempted to correlate the carrier structure with the interaction strength and the performance of SAHCs based on g-C_3N_4. Here, a facile route is introduced to tailor the metal-carrier interaction *via* the copolymerisation of cyanamide with carbon-rich heterocycles (barbituric acid or 2,4,6-triaminopyrimidine), which is applied to synthesise carriers with both bulk and mesoporous morphology. Elemental analysis and ^{13}C magic-angle spinning nuclear magnetic resonance measurements confirm the controlled increase of carbon in the g-C_3N_4 lattice. Palladium is subsequently introduced *via* microwave-irradiation-assisted deposition, which emerges as a highly effective route for the dispersion of single atoms. Analysis by X-ray photoelectron spectroscopy and aberration-corrected scanning transmission electron microscopy evidences the strong dependence of the metal speciation and the oxidation state on the carrier composition, which is rationalised by density functional theory calculations. Stabilising palladium as single atoms is shown to be the key to achieve high alkene selectivity in the continuous flow semi-hydrogenation of 2-methyl-3-butyn-2-ol, while the Pd^{2+}/Pd^{4+} ratio of the SAHCs dominates the reaction rate. The present work demonstrates the importance of tuning the metal-carrier interaction to optimise the catalytic efficiency of SAHCs.

Introduction

Catalytic processes remain heavily reliant on precious metals due to their unparalleled active, selective, and stable character. The development of catalysts based on single atoms is of great interest for the efficient utilisation of these metals.[1-4] Compared to state-of-the-art nanoparticle-based catalysts, which only expose a small fraction of surface atoms that can contribute to the activity, achieving a metal dispersion (defined as the number of surface atoms/total number of atoms) of unity is critical to maximise the catalytic efficiency per atom and reduce the amount of metal required. Enhanced performance has been observed over single atom heterogeneous catalysts (SAHCs) in several relevant processes including hydrogenation,[4] oxidation,[5] and water-gas-shift reactions.[6,7] However, the fabrication of SAHCs is a major challenge because of the tendency of atoms to aggregate into clusters and nanoparticles.[8,9] For this reason, the use of a carrier which provides abundant well defined anchoring sites that can strongly bind metal atoms plays a crucial role in their stabilisation.[10-13]

One material that exhibits a highly attractive set of features as a sustainable carrier is graphitic carbon nitride (g-C_3N_4), which can robustly coordinate metal species within sixfold coordination sites in the lattice.[14] As well as having demonstrated scalability and being composed of inexpensive, nontoxic and earth-abundant elements, it possesses high chemical and thermal stability and can be prepared with flexible morphology and surface area. Besides, the composition of g-C_3N_4 can be easily tuned by using other heteroatom sources.[15] Various metals, including Pd, Pt, Ir, and Ag, have been successfully stabilised as single atoms on this carrier, attaining very reasonable metal contents (*e.g.* 0.5 wt.%).[16] The catalytic superiority of palladium-containing SAHCs based on this carrier has been evidenced in selective hydrogenation reactions, central to the production of many fine chemical and pharmaceutical intermediates, offering an ecological alternative to classical Lindlar-like catalysts that contain high amounts of precious metals and require the use of harmful.[17] Atomically-dispersed Ag-g-C_3N_4 also out-performed the other Ag-based selective hydrogenation catalysts,[18] while single atom platinum catalysts exhibited remarkable photocatalytic hydrogen evolution activity.[19]

Analogous to the widely discussed effects in catalysts based on deposited nanoparticles,[20] in addition to determining the stability, the interaction with the carrier can impact the electronic and related catalytic properties of metal atoms.[21,22] Yet, despite standing at the forefront of their design, few attempts have been made to modify the carrier structure and correlate the impact on the metal binding strength and performance of SAHCs.[26-28] The effect of

the carriers on the electronic properties of the SAHCS is difficult to assess both experimentally and theoretically. Experimentally this is done through the fitting of the XPS signals to species with different oxidation states and thus the shifts are only assigned to charging effects. However, the reduction of the coordination number (from a bulk material to a single atom) also affects the XPS position, and so does the presence of covalency and electric fields. In turn, theoretical models obtain charges through the Bader analysis and they are always lower than the formal ones, and the only XPS shifts are meaningful. In the study of SAHCs, theoretical studies have revealed that some charge transfer and electron sharing occurs when a metal is atomically dispersed on a carriers, these are mapped to the assigned "high-valent metal species" in X-ray photoelectron spectroscopy.[10,23] For example, Pt, Ir, Pd and Ag were all shown to be positively charged when isolated on g-C_3N_4.[16] On other carriers, calculations showed that Pt occupying the positions of Fe atoms on the surface of Fe_2O_3 carry considerable positive charges, which was linked to the remarkable CO oxidation activity of this catalyst.[1] Similarly, Pt was predicted to be trapped as Pt^{2+} on (100) nanofacets of CeO_2 and was detected as Pt^{2+} and Pt^{4+}.[24] On the other hand, Au atoms located at the top sites of Pt_{55} nanoclusters were predicted to be negatively charged.[25] Yet, despite standing at the forefront of their design, few attempts have been made to modify the carrier structure and correlate the impact on the metal binding strength and performance of SAHCs.[26-28]

To gain insight into this crucial aspect, this work studies the effect of modifying the C/N ratio of g-C_3N_4 on the stabilisation, electronic properties and associated catalytic performance of the resulting single atoms. For this purpose, a series of carbon-doped carriers were prepared by copolymerising the conventional cyanamide precursor with two carbon-rich monomers, *i.e.* barbituric acid (BA)[29,30] and 2,4,6-triaminopyrimidine (TAP),[31,32] in different amounts (**Fig. 1**). To assess the effect of the surface area, the carbon-doped materials were prepared in bulk (BCN-BA-*z*) and mesoporous (MCN-BA-*z* and MCN-TAP-*z*) forms. In view of the widely-cited benefits in terms of enhanced size control and uniform dispersion, the introduction of palladium is subsequently approached *via* microwave irradiation assisted deposition. Characterisation by multiple techniques confirms the controlled variation of the carrier structure and the corresponding speciation and oxidation state of palladium. The observations are rationalised based on density functional theory (DFT) calculations to determine the structure of the resulting metal centres. To determine the influence on the catalytic efficiency, the resulting SAHCs were subsequently evaluated in the continuous-flow three-phased semi-hydrogenation of 2-methyl-3-butyl-2-ol, an important reaction in fine chemical and pharmaceutical manufacture.

Experimental

Carrier preparation

Bulk carbon nitride (BCN) was prepared by calcining dicyandiamide (10 g) at 823 K for 4 h (2.3 K min^{-1} ramp rate) under a nitrogen flow (15 cm^3 min^{-1}). Mesoporous carbon nitride (MCN) was prepared by adding cyanamide (2.5 g) to an aqueous dispersion of SiO_2 particles (40 wt.%, 12 nm diameter, Ludox HS-40) with an SiO_2:cynamide mass ratio of 1, and the mixture was stirred at 373 K until the water had completely evaporated. The resulting solids were ground with a mortar and pestle and then calcined as described for BCN. The silica template was subsequently removed by treating the resulting brown-yellow powder in an aqueous solution of NH_4HF_2 (4 M, 16 cm^3 g_{SiO2}^{-1}) for 48 h. The template-free MCN was then filtered, washed thoroughly with distilled water and ethanol and dried at 333 K overnight. Bulk (coded BCN-BA-*z*) and mesoporous (coded MCN-BA-*z* and MCN-TAP-*z*) carbon-doped materials were prepared by copolymerisation of cyanamide with barbituric acid (BA) or 2,4,6-triaminopyrimidine (TAP), following the procedures described above and targeting a molar ratio of 0.9 unless otherwise stated. For reference, BA and TAP were polymerised in pure form (6 g) by calcination under the same conditions resulting in bulk BBA and BTAP materials.

Metal introduction

The incorporation of palladium into carriers was approached by postsynthetic microwave irradiation assisted deposition. The carrier (0.5 g) was firstly dispersed in H_2O (20 cm^3) with the assistance of sonication. Then, a solution of $Pd(NH_3)_4(NO_3)_2$ containing 5 wt.% Pd (50 μL) was added, targeting a metal loading of 0.5 wt.% relative to the carriers. The resulting solution was then placed in a microwave reactor (CEM Discover SP), applying a cyclic program of 15 s irradiation and 3 min cooling with 20 repetitions using a power of 100 W. The resulting powder was washed with distilled water and ethanol and dried at 333 K overnight.

Catalyst characterisation

Elemental analysis of C, H, N and O was determined by infrared spectroscopy using a LECO CHN-900 combustion furnace. Inductively coupled plasma-optical emission spectrometry (ICP-OES) was conducted using a Horiba Ultra 2 instrument equipped with photomultiplier tube detection. The solids were dissolved in a piranha solution and left under sonication until the absence of visible solids in the solution. Powder X-ray diffraction (XRD) was performed in a PANalytical X'Pert PRO-MPD diffractometer operated in Bragg Brentano geometry using Ni-filtered Cu K□ (□ =

0.1541 nm) radiation. Data were recorded in the range of 5-70° 2□ with an angular step size of 0.05° and a counting time of 2 s per step. Nitrogen sorption was measured at 77 K in a Micrometrics 3Flex instrument, after evacuation of the samples at 423 K for 10 h. The pore size distribution was calculated by non-local density functional theory (NLDFT) model applying slit pore geometry. X-ray photoelectron spectroscopy (XPS) was measured in a Physical Electronics Instruments Quantum 2000 spectrometer using monochromatic Al k□ radiation generated from an electron beam operated at 15 kV and 32.3 W. The spectra were collected under ultra-high vacuum conditions (5×10^{-8} Pa) at a pass energy of 50 eV. All spectra were referenced to the C 1*s* peak of adventitious carbon at 284.8 eV. ^{13}C solid-state cross-polarisation/magic angle spinning nuclear magnetic resonance (CP/MAS NMR) spectra were recorded on a Bruker AVANCE III HD NMR spectrometer at a magnetic field of 16.4 T corresponding to a ^{1}H Larmor frequency of 700.13 MHz. A 4 mm double resonance probe head at a spinning speed of 10 kHz was used for all experiments. The ^{13}C spectra were acquired using a cross polarisation experiment with a contact time of 2 ms and a recycle delay of 1 s. A total of 64×10^{3} scans were added for each sample. Between 39×10^{3} and 96×10^{3} scans were acquired depending on the sample. ^{13}C experiments used high-power ^{1}H decoupling during acquisition using a SPINAL-64 sequence. Thermogravimetric (TG) analysis was performed in a Mettler Toledo TGA/DSC 1 Star system. The analysis was performed in air (40 cm^3 min^{-1}), heating the sample from 298 K to 1273 K at a rate of 5 K min^{-1}. Samples for transmission electron microscopy (STEM) studies were prepared by dusting respective powders onto lacey-carbon coated copper grids. Conventional TEM imaging and energy dispersive X-ray spectroscopy (EDX) measurements were performed on a Talos F200X instrument operated at 200 kV and equipped with an FEI SuperX detector. Aberration-corrected (AC-)STEM was performed using an FEI Titan microscope equipped with an XFEG electron source and CEOS probe aberration corrector, was operated at 300 kV with an illumination angle of 20.6 mrad and probe current of ≈60 pA.

Density functional theory

The Vienna *ab-initio* simulation package[x] was employed to model the structure of the Pd SAHCs based on the modified g-C_3N_4 carriers, using the revised Perdew–Burke–Ernzerhof functional.[x] Optimisations for the bulk of these materials and the Pd intercalation structures were performed with the projector augmented wave method to represent core electrons[x] and the valence was expanded in plane waves with a cutoff energy of 450 eV. The C_6N_8 (melon) moieties were built in a graphitic form and the optimised interlayer structure is 3.5 Å. Four layered slabs of the (0001) surface were built with *p* (2 × 2) supercells (**Figure X**). The incorporation of metal atoms, precursors, and dimers were assessed on one side of the slab. Transition states were located by the climbing image-nudged elastic band algorithm.[x]

Catalyst testing

The hydrogenation of 2-methyl-3-butyl-2-ol (Acros Organics, 98%) was carried out in a continuous-flow flooded-bed micro-reactor (ThalesNano H-Cube Pro™), in which the liquid feed (containing 5 vol.% of substrate and toluene (Fischer Chemicals, 99.95%) and gaseous hydrogen (generated *in situ* by Millipore water electrolysis) flow concurrently upward through a cylindrical cartridge (3.5 mm internal diameter) containing a fixed bed of catalyst (0.1 g) and silicon carbide (0.12 g) particles, both with a size of 0.2-0.4 mm. The reactions were conducted at various conditions of temperature (303-363 K), total pressure (1-8 bar), liquid (1 cm^3 min^{-1}) and H_2 (40 cm^3 min^{-1}) flow rates. The products were collected every 15 min after reaching steady state and analysed offline using a gas chromatograph (HP-6890) equipped with a HP-5 capillary column and a flame ionisation detector. The conversion (*X*) of the substrate was determined as the amount of reacted substrate divided by the amount of substrate at the reactor inlet. The selectivity (*S*) to each product was quantified as the amount of the particular product divided by the amount of reacted substrate. The reaction rate (*r*) was expressed as mole of product per mole of Pd and unit of time.

Results and Discussion

Carrier properties

The preparation of carbon-doped g-C_3N_4 carriers was approached by copolymerising the conventional cyanamide precursor with barbituric acid (BA) or 2,4,6-triaminopyrimidine (TAP). These compounds both contain carbon-rich heterocycles with respect to the six-membered ring of melamine, the smallest aromatic unit of the condensed structure, and ideally have compatible functionality to copolymerise with this molecule to form the standard tri-*s*-triazine units *via* the elimination of ammonia or water. To demonstrate the flexibility of this approach and to study the impact of surface area, carbon-doped carriers have been prepared in both bulk and mesoporous forms, the latter obtained by applying a colloidal silica template during the synthesis. The resulting samples are coded *x*-*y*-*z*, where *x* denotes the carrier morphology (bulk - BCN or mesoporous – MCN), *y* corresponds to the dopant applied (BA or TAP) and *z* indicates the cyanamide/dopant mass ratio (0.02, 0.2 or 0.9). For reference purposes the stoichiometric g-C_3N_4 carrier was also synthesised with bulk (BCN) and mesoporous (MCN) morphology and the individual dopants were also polymerised in bulk form leading to the BBA and BTAP materials.

Various techniques were applied to characterise the successful modification of the carrier properties. Elemental analysis confirmed the increased carbon upon introduction of BA or TAP during the synthesis (**Table S1**), the C/N ratio rising from 0.66 in the stoichiometric materials to close to 1 in the carbon-doped analogues. In general, the increased oxygen content of the mesoporous carriers is expected due to the higher surface area of these materials, but slightly higher oxygen contents are also observed on application of BA as a dopant. Comparison of the X-ray diffraction (XRD) patterns of the mesoporous (**Fig. 2a**) and bulk (**Fig. S1a**) carriers reveals that the incorporation of carbon was accompanied by a disturbance of the crystalline structure. In particular, increasing the cyanamide/dopant ratio was associated with a broadening and reduced intensity of the (002) stacking reflection at 2□ = 27.3° (**Fig. S2**). Moreover, the reflection at 2□ = 13.1° corresponding to the in-plane order of tri-*s*-triazine units within the g-C_3N_4 sheets, is not visible in the carbon-doped samples, suggesting an increased distortion of g-C_3N_4 stacking layers and a decreased crystallite size.[33] The slight shift and broadening of the reflection at 2□ = 27.3° indicate a small concomitant increase in the interlayer stacking from 0.326 nm in MCN to 0.332 nm in MCN-BA-0.9.[32] In fact, the substitution of one or more nitrogen atoms in the framework of g-C_3N_4 leads to a decreased strength of hydrogen bonds, which is known to reduce the stability and structural regularity in g-C_3N_4 materials.[30] Comparatively, the observation of a single broad reflection at 2□ = 27.3° in the materials obtained upon the direct thermal condensation of barbituric acid (BBA) or 2,4,6-triaminopyrimidine (BTAP) indicate that they adopt a layered structure similar to that of the conventional graphitic carbon nitride (BCN).

As evidenced by nitrogen sorption, MCN-BA-0.9 and MCN-TAP-0.9 display an enhanced surface area compared to pure MCN (**Table S1**), which is consistent with the reduced crystalline order. The prominent hysteresis loops observed in all isotherms evidence the presence of connected spherical or cylinder mesopores (**Fig. 2b**). Corresponding pore size distributions (**Fig. 2b**, inset) display two pronounced peaks, centred at 1.5 and 10 nm, the latter close to the size of the SiO_2 template. As expected, the BCN and BTAP carriers exhibit surface areas lower than 10 $m^2 g^{-1}$ consistent with the densification of the polymerised structures in the absence of a template. In comparison, BBA and BCN-BA-0.9 display relatively high specific surface areas of 45 and 48 $m^2 g^{-1}$, respectively, with a hysteresis loop at p/p_0 = 0.3-0.9, suggesting the presence of smaller crystalline domains and/or a higher number of defects in these samples (**Fig. S1b**). The thermal stability was improved after carbon introduction. For example, the temperature for 50% weight loss of carbon-doped g-C_3N_4 is 50 K higher compare to MCN (**Fig. 2c** and **S2)**, which also applies for the bulk carriers (**Fig. S1c**).

To further confirm the successful incorporation of carbon into the g-C_3N_4 lattice, the mesoporous samples were studied by nuclear magnetic resonance (NMR) and X-ray photoelectron (XPS) spectroscopy. The two main signals at 164 and 157 ppm in the ^{13}C MAS NMR spectrum of MCN are attributed to $CN_2(NH_x)$ and CN_3 moieties, respectively (**Fig. 2d**).[34] The gradual coalescence of these peaks with increased amount of BA or TAP (**Fig. S3**) in the spectra can be related to the interruption of the tri-*s*-triazine moieties or the disturbance of the structure. In addition, a new peak centred at 95 ppm appears, which reflects the desired incorporation of -C-C=N- units into the framework.[30] Consistently, MCN-BA-0.9 and MCN-TAP-0.9 samples evidence a strong peak at 287.3 eV in the C 1*s* XPS spectra (**Fig. 2e**) that is attributed to the -C-C=N-bonds of newly incorporated carbon atoms,[35] while the peak at 284.8 eV that represents C-C bond formation also increases. The latter could result from the formation of an amorphous carbon phase during the polymerisation. The existence of the tri-*s*-triazine units was confirmed by the presence of the peak at 288.1 eV (CN_3).[36] Deconvolution of N 1*s* XPS spectra (**Fig. 2f**) identifies the presence of nitrogen species, typical for the g-C_3N_4 structure. Three main peaks at 398.6 eV (ring nitrogen, C-N=C), 399.5 eV (tertiary nitrogen, NC_3) and 400.6 eV (NH_x groups) are observed in all spectra. The presence of tertiary nitrogen and the C-N=C/NC_3 ratio of 6 for MCN carrier confirms that the structure is based on tri-*s*-triazine building block.[37] The C-N=C/NC_3 ratio drops to 3.7 and 3.5 for MCN-TAP-0.9 and MCN-BA-0.9, respectively, indicating a decreased amount of the ring nitrogen in the carbon-doped carriers and evidencing the successful substitution of nitrogen by carbon in the sixfold cavity of the g-C_3N_4 structure.

As illustrated for selected samples in **Fig. 3**, the copolymerisation of cyanamide with up to 1:1 molar ratio of BA or TAP does not radically alter the carrier morphology. All mesoporous carriers exhibit the extensive presence of spherical mesopores reflecting the geometry of 12 nm colloidal silica template (**Fig. S4**). On the other hand, MCN-TAP-0.9 sample shows mixed morphology: mesoporous sheets interweave with non-porous ones. Low surface area carriers exhibit large irregularly-shaped nonporous particles.[38] Note that the observation of numerous mesopores and macropores in bulk BBA prepared from pure BA agrees with the higher surface area of this material.

Palladium stabilisation on the carriers

The metal speciation of the Pd-containing catalysts was carefully examined by aberration-corrected (AC-)STEM, confirming the absence of Pd nanoparticles in any of the catalysts based on the carbon-doped carriers (**Table S2**). However, some metal clusters of ~1 nm were observed in Pd-BCN-BA-0.9 (**Fig. S6** and **S7**). It is noteworthy that the absence of metal agglomerates was also confirmed on the Pd-BCN carrier. Attempts at metal introduction *via* wet deposition previously led to significant amounts of nanoparticles on BCN, attributed to the low surface area of this

carrier (9 cm^3 g^{-1}).[16] Here, the use of microwave-irradiation-assisted deposition enables the stabilisation of single atoms on low surface area carriers with the metal loading up to 0.5 wt.%, demonstrating the enhanced efficiency of this route. Thus, the surface area is not the most crucial factor in determining the metal speciation in this study. On the contrary, Pd clusters and small nanoparticles were evidenced in Pd-BBA, which has the highest surface area of the bulk carriers (61 m^2 g^{-1}). Instead, differences in the metal speciation can be explained by the structure and binding strength of the coordination sites within the material. Since the polymerisation of BA and TAP does not result in well-defined latticed based on tri-*s*-triazine, these carriers are more like nitrogen-doped carbon materials without the 'nitrogen pockets' that host the Pd atoms as in the cases of other carriers.

The impact of modifying the carrier composition on the oxidation state of palladium in the resulting catalysts was further assessed by XPS (**Fig. 5a** and **S8**), which can give an indication of the strength of the interaction. The Pd 3*d* spectra of all samples can be deconvoluted into two peaks at 338.5 eV and 336.9 eV, which are tentatively assigned to Pd^{4+} and Pd^{2+} based on the shifts expected for the bulk compounds, respectively. Notably, no peak corresponding to metallic Pd around 335 eV was observed in any of the spectra.[39] Interestingly, significant variation is observed in the relative peak intensity, the Pd^{2+}/Pd^{4+} ratio changing from 0.24 for Pd-MCN-BA-0.9 to 1.04 for Pd-MCN-TAP-0.9, while Pd-MCN shows intermediate value 0.53 (**Table S2**). Replacing the nitrogen atoms with carbon in the stoichiometric g-C_3N_4 structure, a weaker metal-carrier interaction and thus a higher Pd^{2+}/Pd^{4+} ratio is expected, as in the case of Pd-MCN-TAP-0.9. In contrast to this, a lower Pd^{2+}/Pd^{4+} ratio was observed in Pd-MCN-BA-0.9, tentatively explained by the higher oxygen content in the carrier (**Table S1**, 7.2 and 5.4 mol% for MCN-BA-0.9 and MCN-TAP-0.9 respectively). Since oxygen is more electronegative than nitrogen and carbon, it strongly interacts with metal atoms and thus an enhanced metal-carrier interaction takes place (**Fig. 5b**). Among the nonporous C-doped catalysts, Pd-BCN-BA-0.9 has the highest Pd^{2+}/Pd^{4+} ratio. Even though the C/N in MCN-BA-0.9 and BCN-BA-0.9 is similar (1.02 and 0.98, respectively) the difference in oxygen amount is clearly observed and shows the same impact as described above: a reduced amount of oxygen (4.3 mol%) in the carrier is associated with a weaker metal-carrier interaction. The absence of the metallic Pd signal in the Pd 3*d* spectra of Pd-BBA and Pd-BTAP conflicts with the presence of small clusters as confirmed by STEM analysis, which can be explain by bathochromic shift due to the quantum effects appears for particles smaller than 2 nm.[40] These results demonstrate the tuneable nature of metal-carrier interaction depending on the relative ratio between carbon, nitrogen and oxygen amount presenting in the carrier material.

Calculation of the interaction strength

Theoretical part, plus relevant figures.

Catalytic performance

To unravel the structure-performance relationship, selected materials were evaluated in the continuous-flow semi-hydrogenation of 2-methyl-3-butyn-2-ol. Interestingly, despite exhibiting a similar chemical composition, porosity and crystalline order, Pd-MCN-TAP-0.9 displayed significantly enhanced activity with respect to Pd-MCN-BA-0.9 (**Fig. 6**). Comparison of the performance at 343 K and 5 bar reveals a 3.6 times higher reaction rate over Pd-MCN-TAP-0.9 than Pd-MCN-BA-0.9 and 1.2 times that of the reference Pd-MCN. Nonetheless, these samples all demonstrate a high selectivity to 2-methyl-3-buten-2-ol (> 95%) consistent with the exclusive presence of single atoms. The finding can be ascribed to the variation of the metal-carrier interaction in these SAHCs. In agreement with the XPS analysis, the activity of the catalysts is determined by the amount of lower valent Pd^{2+}, the higher the Pd^{2+}/Pd^{4+} ratio the weaker metal-carrier interaction, and thus the improved catalytic efficiency (**Fig. 7**). This was further supported by the performance of Pd-BCN-BA-0.9. Possessing the highest Pd^{2+}/Pd^{4+} ratio of 0.75 among the bulk catalysts, Pd-BCN-BA-0.9 exhibits the best semi-hydrogenation activity and even better than Pd-MCN-TAP-0.9. This is probably due to the concentrated Pd atoms on the surface of the bulk carriers, suggesting that high surface area may not be necessary if the metal species can exist as single atoms in the catalysts. This finding hints the importance of the metal-carrier interaction on the design of the highly efficient SAHCs. Considering the effect of metal aggregation, Pd-BBA exhibits a comparable activity to Pd-BCN-BA-0.9, while the selectivity to alkene drops sharply over the temperature of 323 K. These results indicate a subtle difference in the population of single atoms and nanoclusters between the samples which is difficult to quantify at the moment.

Conclusions

This study has assessed the impact of varying the elemental composition of carbon nitride on the stabilisation and catalytic efficiency of palladium species on this carrier. Controlled modification of the carrier structure could be achieved by the copolymerisation of cyanamide with carbon-rich heterocycles in both bulk and mesoporous forms. The substitution of nitrogen by carbon in the lattice was confirmed by elemental analysis, XPS and ^{13}C NMR spectroscopy and was found to concomitantly enhance the surface area and thermal stability. Microwave irradiation assisted deposition was shown to be an effective route for dispersing metals as single atoms even on low surface area carriers. As evidenced by XPS and AC-STEM, both the speciation and oxidation state of palladium was influenced by the

specific dopant applied. The incorporation of 2,4,6-triaminopyrimidine led to the weakening of the metal-carrier interaction expected due to the reduced coordination number of the binding sites, but an increased binding strength was observed upon incorporation of barbituric acid, attributed to the higher electronegativity of the lattice due to the presence of oxygen. The metal oxidation state in the resulting catalysts was found to be an important indicator for the semi-hydrogenation of 2-methyl-3-butyn-2-ol with an enhanced catalytic efficiency observed over catalysts containing higher fractions of lower-valence metal. The findings demonstrate the possibility of improving the efficiency of SAHCs by tailoring the carrier properties.

Acknowledgements

This research has received funding from the Swiss National Science Foundation (Grant No. 200021-169679). Dr Réne Verel (ETH Zurich) is thanked for assistance with ^{13}C MAS-NMR. ScopeM at ETH Zurich is acknowledged for providing access to its facilities.

Figures and tables

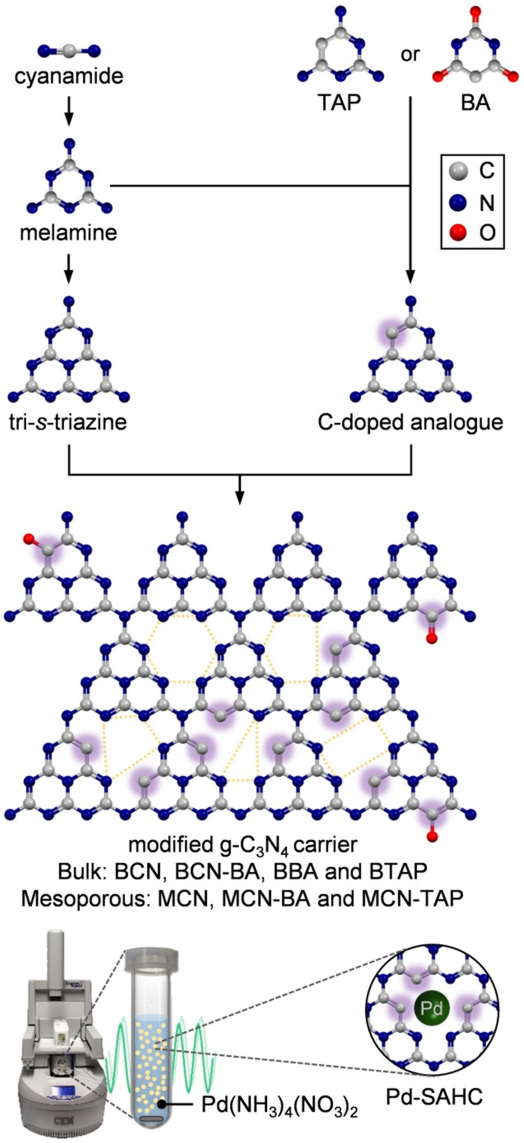

Fig. 1 Steps of the polymerisation of carbon-doped g-C_3N_4 structure. The newly incorporated carbon atoms are highlighted. Yellow dashed lines illustrate the coordination sphere of metal atoms in Pd-SAHCs. The figure illustrates the microwave irradiation assisted metal deposition method.

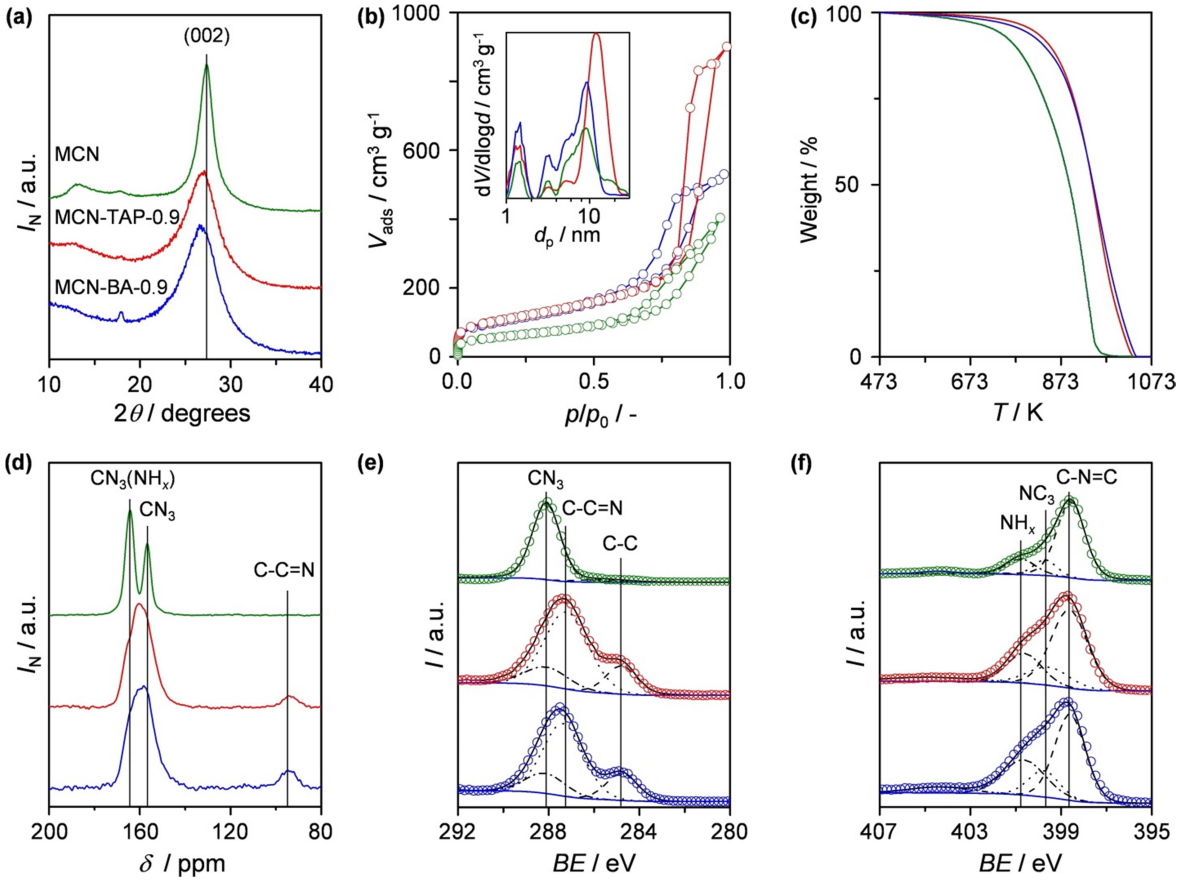

Fig. 2 (a) XRD patterns, (b) N_2 isotherms and corresponding NLDFT pore size distributions (inset), (c) TGA profiles, (d) ^{13}C MAS NMR spectra, (e) C 1*s* XPS spectra and (f) N 1*s* XPS spectra of the stoichiometric and carbon-doped mesoporous g-C_3N_4 carriers. In (e,f), solid black lines show the result of fitting the raw data (open symbols), the dashed lines correspond to the individual peaks after deconvolution. Blue lines indicate the background applied. Vertical lines correspond to the deconvoluted components, which are tentatively assigned based on the shifts expected for bulk species.

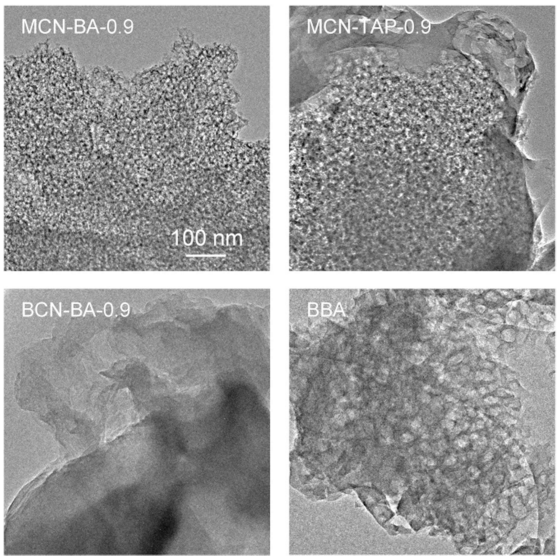

Fig. 3 BF-TEM images of mesoporous and bulk g-C_3N_4 copolymerised with BA or TAP. The 100 nm scale bar applies to all images.

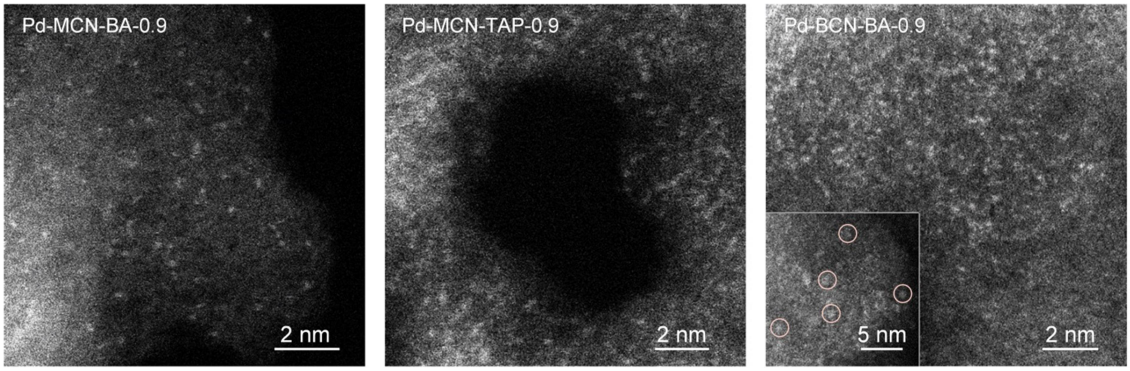

Fig. 4 AC-STEM images of the metal speciation in Pd-containing SAHCs based on the carbon-doped carriers.

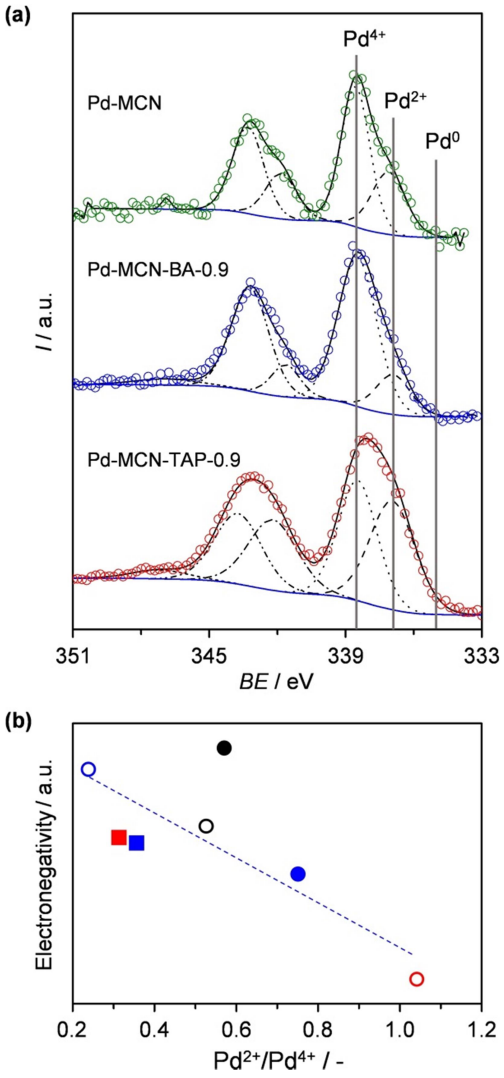

Fig. 5 (a) Comparison of the Pd 3*d* core level XPS spectra of the catalysts based on the mesoporous carriers. Solid black lines show the result of fitting the raw data (open symbols), the dashed lines correspond to the individual peaks after deconvolution. Blue lines indicate the background applied. Vertical grey lines correspond to the deconvoluted components, which are tentatively assigned based on the shifts expected for bulk species. (b) Correlation of the electronegativity of the carrier framework with the Pd^{2+}/Pd^{4+} ratio. The catalysts based on bulk carriers are coded in solid symbols, mesoporous are in open symbols, red colour indicated copolymerisation with TAP, blue colour refers to BA, while MCN and BCN are marked in black. Samples in squares corresponds to the catalysts based on BBA and TAP.

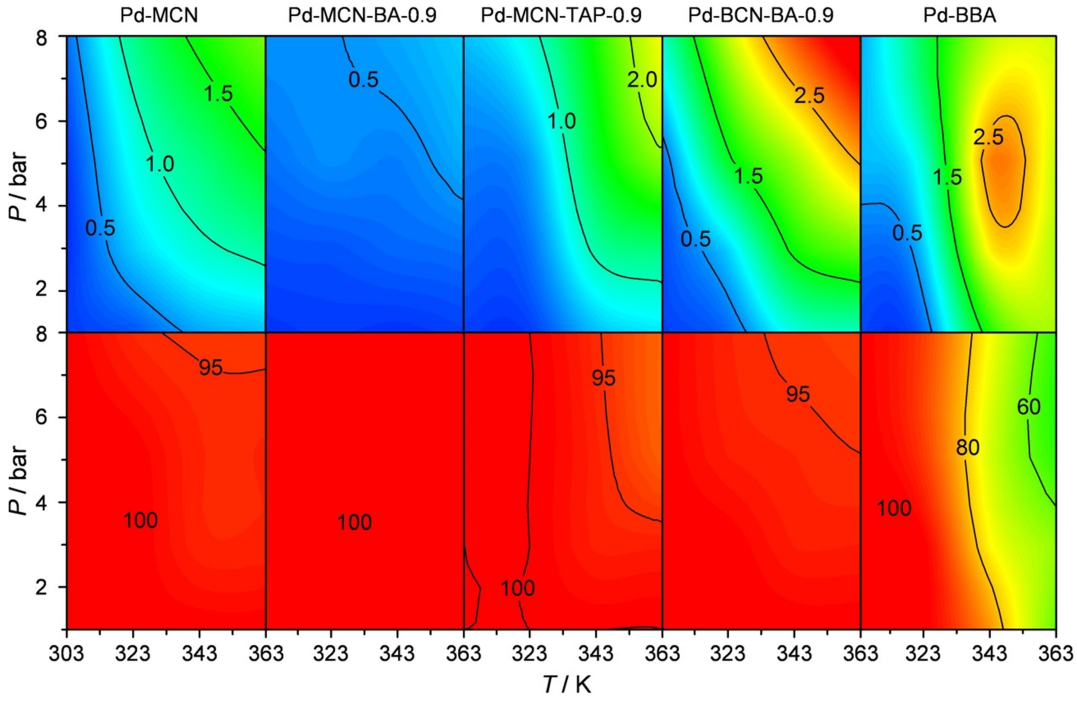

Fig. 6 Reaction rate (top row) of 2-methyl-3-butyn-2-ol (in 10^3 $mol_{2\text{-methyl-3-buten-2-ol}}$ mol_{Pd}^{-1} h^{-1}) hydrogenation and selectivity (in %) to 2-methyl-3-buten-2-ol (bottom row) at different temperature and pressure over Pd-based catalysts on g-C_3N_4 and BBA carriers. The contour plots were obtained through spline interpolation of 14 experimental points. Reaction conditions: W_{cat} = 0.1 g, F_L (2-methyl-3-butyn-2-ol + toluene) = 1 cm^3 min^{-1} and F_G (H_2) = 36 cm^3 min^{-1}

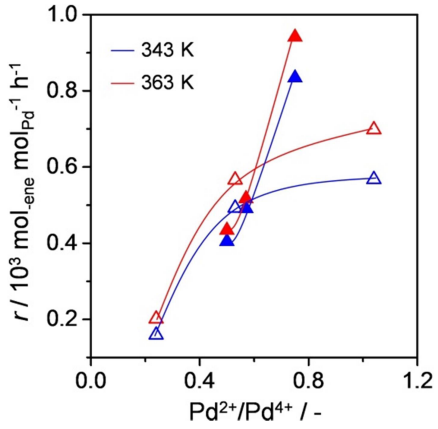

Fig. 7 Correlation of the semi-hydrogenation reaction rate with Pd^{2+}/Pd^{4+} ratio of the mesoporous (open symbols) and nonporous (solid symbols) catalysts. The reaction was carried out at the pressure of 1 bar.

References

1. B. Qiao, A. Wang, X. Yang, L. F. Allard, Z. Jiang, Y. Cui, J. Liu, J. Li and T. Zhang, *Nat. Chem.*, 2011, **3**, 634-641.
2. X.-F. Yang, A. Wang, B. Qiao, J. Li, J. Liu and T. Zhang, *Acc. Chem. Res.*, 2013, **46**, 1740-1748.
3. S. Liang, C. Hao and Y. Shi, *ChemCatChem*, 2015, **7**, 2559-2567.
4. G. Kyriakou, M. B. Boucher, A. D. Jewell, E. A. Lewis, T. J. Lawton, A. E. Baber, H. L. Tierney, M. Flytzani-Stephanopoulos and E. C. H. Sykes, *Science*, 2012, **335**, 1209-1212.
5. M. Moses-DeBusk, M. Yoon, L. F. Allard, D. R. Mullins, Z. Wu, X. Yang, G. Veith, G. M. Stocks and C. K. Narula, *J. Am. Chem. Soc.*, 2013, **135**, 12634-12645.
6. Q. Fu, H. Saltsburg and M. Flytzani-Stephanopoulos, *Science*, 2003, **301**, 935-938.
7. Y. Zhai, D. Pierre, R. Si, W. Deng, P. Ferrin, A. U. Nilekar, G. Peng, J. A. Herron, D. C. Bell, H. Saltsburg, M. Mavrikakis and M. Flytzani-Stephanopoulos, *Science*, 2010, **329**, 1633-1636.
8. S. Sun, G. Zhang, N. Gauquelin, N. Chen, J. Zhou, S. Yang, W. Chen, X. Meng, D. Geng, M. N. Banis, R. Li, S. Ye, S. Knights, G. A. Botton, T.-K. Sham and X. Sun, *Sci. Rep.*, 2013, **3**, 1775.
9. A. Uzun, V. Ortalan, Y. Hao, N. D. Browning and B. C. Gates, *ACS Nano*, 2009, **3**, 3691-3695.
10. M. Yang, J. Liu, S. Lee, B. Zugic, J. Huang, L. F. Allard and M. Flytzani-Stephanopoulos, *J. Am. Chem. Soc.*, 2015, **137**, 3470-3473.
11. A. L. Yakovlev, K. M. Neyman, G. M. Zhidomirov and N. Rösch, *J. Phys. Chem.*, 1996, **100**, 3482-3487.
12. J. Lin, A. Wang, B. Qiao, X. Liu, X. Yang, X. Wang, J. Liang, J. Li, J. Liu and T. Zhang, *J. Am. Chem. Soc.*, 2013, **135**, 15314-15317.
13. H. Wei, X. Liu, A. Wang, L. Zhang, B. Qiao, X. Yang, Y. Huang, S. Miao, J. Liu and T. Zhang, *Nat. Commun.*, 2014, **5**, 5634.
14. Z. Zhao, Y. Sun and F. Dong, *Nanoscale*, 2015, **7**, 15-37.
15. Y. Zheng, J. Liu, J. Liang, M. Jaroniec and S. Z. Qiao, *Energy Environ. Sci.*, 2012, **5**, 6717-6731.
16. Z. Chen, S. Mitchell, E. Vorobyeva, R. K. Leary, R. Hauert, T. Furnival, Q. M. Ramasse, J. M. Thomas, P. A. Midgley, D. Dontsova, M. Antonietti, S. Pogodin, N. López and J. Pérez-Ramírez, *Adv. Funct. Mater.*, 2017, **27**, 1605785.
17. X. Huang, Y. Xia, Y. Cao, X. Zheng, H. Pan, J. Zhu, C. Ma, H. Wang, J. Li, R. You, S. Wei, W. Huang and J. Lu, *Nano Res.*, 2017, doi:10.1007/s12274-016-1416-z.
18. Z. Chen, S. Pronkin, T.-P. Fellinger, K. Kailasam, G. Vilé, D. Albani, F. Krumeich, R. Leary, J. Barnard, J. M. Thomas, J. Pérez-Ramírez, M. Antonietti and D. Dontsova, *ACS Nano*, 2016, **10**, 3166-3175.
19. X. Li, W. Bi, L. Zhang, S. Tao, W. Chu, Q. Zhang, Y. Luo, C. Wu and Y. Xie, *Adv. Mater.*, 2016, **28**, 2427-2431.
20. S. J. Tauster, S. C. Fung, R. T. K. Baker and J. A. Horsley, *Science*, 1981, **211**, 1121-1125.
21. G. N. Vayssilov, Y. Lykhach, A. Migani, T. Staudt, G. P. Petrova, N. Tsud, T. Skála, A. Bruix, F. Illas, K. C. Prince, V. Matolín, K. M. Neyman and J. Libuda, *Nat. Mater.*, 2011, **10**, 310-315.
22. A. Kumar and V. Ramani, *ACS Catal.*, 2014, **4**, 1516-1525.
23. G. Vilé, D. Albani, M. Nachtegaal, Z. Chen, D. Dontsova, M. Antonietti, N. López and J. Pérez-Ramírez, *Angew. Chem. Int. Ed.*, 2015, **54**, 11265-11269.
24. A. Bruix, Y. Lykhach, I. Matolínová, A. Neitzel, T. Skála, N. Tsud, M. Vorokhta, V. Stetsovych, K. Ševčíková, J. Mysliveček, R. Fiala, M. Václavů, K. C. Prince, S. Bruyère, V. Potin, F. Illas, V. Matolín, J. Libuda and K. M. Neyman, *Angew. Chem. Int. Ed.*, 2014, **53**, 10525-10530.
25. H. Zhang, T. Watanabe, M. Okumura, M. Haruta and N. Toshima, *Nat. Mater.*, 2012, **11**, 49-52.
26. F. Besenbacher, I. Chorkendorff, B. S. Clausen, B. Hammer, A. M. Molenbroek, J. K. Nørskov and I. Stensgaard, *Science*, 1998, **279**, 1913-1915.
27. F. R. Lucci, J. Liu, M. D. Marcinkowski, M. Yang, L. F. Allard, M. Flytzani-Stephanopoulos and E. C. H. Sykes, *Nat. Commun.*, 2015, **6,** 8550.
28. M. Mavrikakis, P. Stoltze and J. K. Nørskov, *Catal. Lett.*, 2000, **64**, 101-106.
29. M. Shalom, M. Guttentag, C. Fettkenhauer, S. Inal, D. Neher, A. Llobet and M. Antonietti, *Chem. Mater.*, 2014, **26**, 5812-5818.
30. J. Zhang, X. Chen , K. Takanabe, K. Maeda, K. Domen, J. D. Epping, X. Fu, M. Antonietti and X. Wang, *Angew. Chem. Int. Ed.*, 2010, **49**, 441-444.
31. W. Ho, Z. Zhang, W. Lin, S. Huang, X. Zhang, X. Wang and Y. Huang, *ACS Appl. Mater. Interfaces*, 2015, **7**, 5497-5505.
32. M. K. Bhunia, K. Yamauchi and K. Takanabe, *Angew. Chem.*, 2014, **126**, 11181-11185.
33. F. Goettmann, A. Fischer, M. Antonietti and A. Thomas, *Angew. Chem. Int. Ed.*, 2006, **45**, 4467-4471.
34. B. V. Lotsch, M. Döblinger, J. Sehnert, L. Seyfarth, J. Senker, O. Oeckler and W. Schnick, *Chem. Eur. J.*, 2007, **13**, 4969-4980.
35. M. K. Bhunia, S. Melissen, M. R. Parida, P. Sarawade, J.-M. Basset, D. H. Anjum, O. F. Mohammed, P. Sautet, T. Le Bahers and K. Takanabe, *Chem. Mater.*, 2015, **27**, 8237-8247.
36. A. Thomas, A. Fischer, F. Goettmann, M. Antonietti, J.-O. Müller, R. Schlögl and J. M. Carlsson, *J. Mater. Chem.*, 2008, **18**, 4893-4908.
37. Ch. Fettkenhauer, G. Clavel, K. Kailasam, M. Antonietti and D. Dontsova, *Green Chem.*, 2015, **17**, 3350-3361.
38. K. Fuku, R. Hayashi, S. Takakura, T. Kamegawa, K. Mori and H. Yamashita, *Angew. Chem. Int. Ed.*, 2013, **52**, 7446-7450.
39. L. S. Kibis, A. I. Stadnichenko, S. V. Koscheev, V. I. Zaikovskii and A. I. Boronin, *J. Phys. Chem. C*, 2012, **116**, 19342-19348.
40. Y. Sun, Y. Wang, J. S. Pan, L.-l. Wang and C. Q. Sun, *J. Phys. Chem. C*, 2009, **113**, 14696-14701.